Geophysical Journal International

Geophys. J. Int. (2024) **236,** 1484–1498
Advance Access publication 2023 December 21
GJI Geodynamics and Tectonics

https://doi.org/10.1093/gji/ggad489

Spatio-temporal variability in slab temperature within dynamic 3-D subduction models

Valeria Turino and Adam F. Holt

Department of Marine Geosciences; Rosenstiel School of Marine, Atmospheric, and Earth Science; University of Miami, FL 33149-1031, USA. E-mail: valeria.turino@earth.miami.edu

Accepted 2023 December 19. Received 2023 November 22; in original form 2023 August 16

SUMMARY

Spatio-temporal variability in arc geochemistry and the conditions recorded by exhumed rocks suggest subduction zone thermal structure evolves in time and along-strike. Although much effort has been dedicated to studying subduction zone thermal structure, we lack an understanding of spatio-temporal temperature variability during time-dependent subduction. We model 3-D, dynamic subduction and examine the time evolution of the along-strike temperature difference of the slab's upper surface ('slab-top') at the centre relative to the edge of the subduction zone. We examine this slab-top temperature variability for subduction systems of different widths and with different plate mobilities (i.e. fixed versus free subducting and overriding plates). In all of our models, the main control on slab-top temperature is convergence rate; either by simply controlling the rate of slab sinking or via the effect it has on the decoupling depth (DD). In the early stages of subduction, more rapid convergence at the plate centre produces a cooler slab relative to warmer slab edges. For mature subduction, this flips; a shallower DD at the slab centre produces warmer temperatures with respect to the edge. Importantly, our maximum along-strike temperature changes are reduced ($\leq$50 °C) relative to previous kinematically driven modelling studies, due to a reduced role for slab-top heating via toroidal flow. Our dynamic subduction models, therefore, point towards a strong time dependence in the sense of along-strike temperature variation, but with relatively low absolute values in geometrically simple subduction zones.

Key words: Numerical modelling; Continental margins: convergent; Dynamics of lithosphere and mantle; Subduction zone processes.

1 INTRODUCTION

Subduction zone thermal structure regulates a plethora of important geological processes, including arc volcanism (e.g. Katili 1975) and the metamorphism of downgoing rocks (e.g. Ernst 1973). At many subduction zones, these geological products suggest significant spatial and temporal variability in subduction zone temperature fields: The pressure–temperature (*P–T*) conditions of exhumed metamorphic rocks can record significant variation in thermal history between units that are spatially close (e.g. Platt 1975; O'Brien 1997), and exhumed rocks associated with oceanic terrains suggests highly variable *P–T* conditions during different stages of subduction, with typically warmer conditions during the earliest phases of subduction that later transition to colder conditions (e.g. Platt 1975; Cloos 1985; Krebs *et al.* 2011; Agard *et al.* 2018). The production rate and geochemistry of arc magma has also been shown to be time-dependent (e.g. Tupinambá *et al.* 2012; Elburg & Foden 1998) and exhibit along-arc variability which, at numerous subduction zones, has been attributed to thermal variability of the slab and/or mantle wedge (e.g. Portnyagin & Manea 2008; Bai *et al.* 2020).

Such observations suggest that the thermal conditions of slabs are both temporally and spatially variable. Numerical subduction models are often used to investigate the mechanisms behind slab temperature variability. Previous numerical models have shown that basic subduction zone properties—convergence rate, slab dip and downgoing plate age—exert a first-order control on temperatures along the surface of the slab or the 'slab-top' (e.g. Peacock 1996; Peacock & Wang 1999; Van Keken *et al.* 2002). To this end, the product of these three properties, termed the 'thermal parameter' (Kirby *et al.* 1996), has been utilized as a first-order indicator of slab-top temperatures with low and high values corresponding to warm and cold subduction zones, respectively (e.g. van Keken *et al.* 2011).

In this modelling study, we utilize and extend these fundamental principles to probe the thermal evolution of 3-D subduction zones. Previous numerical subduction models, which specifically target subduction zone thermal structure, are either dynamic but 2-D (e.g. Kincaid & Sacks 1997; Holt & Condit 2021; Zhou & Wada 2021) or are 3-D but kinematically impose the behaviour of part of the subduction system (e.g. Bengtson & van Keken 2012;

Morishige & van Keken 2014; Wada *et al.* 2015; Plunder *et al.* 2018). Kinematically driven thermal models, in which quantities such as convergence rate and slab geometry are prescribed at all times, are well suited to describe specific Earth subduction zones with known kinematic properties. When constructed in 3-D, such models have illuminated a range of subduction processes that can produce along-strike temperature variability within time-invariant subduction zones: for example mantle flow regime and vigour (Kincaid & Griffiths 2004; Bengtson & van Keken 2012; Wada *et al.* 2015; Wada 2021), along-strike variability in slab-rollback rate and convergence rate (Bengtson & van Keken 2012; Ji *et al.* 2017; Plunder *et al.* 2018), trench obliquity and decoupling depth (Morishige & van Keken 2014) and complex plate and slab geometries (Ji *et al.* 2016). These studies highlight a wide range of along-strike slab-top temperature changes, spanning values from 30 °C (Plunder *et al.* 2018) to 200 °C (e.g. Bengtson & van Keken 2012; Wada *et al.* 2015; Ji *et al.* 2016; Plunder *et al.* 2018), with intermediate values of ∼100 °C (e.g. Morishige & van Keken 2014; Kincaid & Griffiths 2004) as a result of the above-mentioned processes. These studies, however, do not account for temporal variability.

Modelling the temporal evolution of subduction zone thermal structure has been mainly limited to 2-D (e.g. Kincaid & Sacks 1997; Holt & Condit 2021; Zhou & Wada 2021). By enabling the subduction system to evolve self-consistently in 'dynamic' models, Holt & Condit (2021) demonstrated that the slab-top cools during the early and intermediate phases of subduction, in basic agreement with peak *P–T* conditions extracted from the exhumed rock record. The primary drivers of this thermal evolution are temporal changes in convergence rate and decoupling depth (DD). The DD marks the downdip transition from cold and stiff material directly above the slab (i.e. from the forearc region of the upper plate) to hot and warm material above the slab (i.e. from the circulating portion of the mantle wedge). From a mechanical perspective, this corresponds to a transition from a slab that is decoupled from overlying material, and so does not drag the forearc down the subduction zone, to a slab that is coupled to the weak mantle wedge and hence exerts shear stresses that drive wedge flow (Furukawa 1993). In kinematically driven thermal models, it is typically held fixed at ≈80 km depth (Wada & Wang 2009; Syracuse *et al.* 2010). Dynamic models of the type considered here, and within which the DD evolves self-consistently (albeit up to some maximum, imposed depth), therefore enable this additional mechanism to drive time-dependent slab thermal structure.

In this work, we use a 3-D and dynamic subduction modelling approach to explore how slab-top temperature (i.e. the temperature extracted at the top of the oceanic crust comprising the uppermost layer of the slab) varies in the trench-parallel direction, and how this variation evolves over tens of millions of years. This approach allows us to simultaneously account for the temporal and spatial variability suggested by natural observations and, in turn, probe the physical mechanisms responsible for such variability in our models. We model dynamic subduction using the ASPECT finite element code (Kronbichler *et al.* 2012; Heister *et al.* 2017; Bangerth *et al.* 2019). We examine the effect of plate/slab width (1000 km, 2000 km, infinite) and plate mobility ('fixed' versus free' subducting and overriding plates) on the dynamics of subduction and how these variations manifest in spatio-temporal slab-top temperature changes. We extract slab-top temperatures for three different stages (free sinking, interaction with the lower mantle and mature subduction) and depths (60, 130 and 200 km), and focus on the role of convergence rate, mantle flow pattern and DD variability in driving slab temperature variability. Finally, we place our results into the context of previous modelling and observational studies that target subduction zone thermal structure.

2 METHODS

2.1 Governing equations

We model subduction in a 3-D Cartesian domain using the finite-element code ASPECT, version 2.1.0 (Kronbichler *et al.* 2012; Heister *et al.* 2017; Bangerth *et al.* 2019). We solve the conservation equations for mass (eq. 1), momentum (eq. 2) and energy (eq. 3) for a viscous, incompressible Boussinesq fluid with no inertia, shear heating or internal heating:

$$\nabla \cdot \mathbf{v} = 0 \tag{1}$$

$$-\nabla \cdot 2\eta\dot{\varepsilon} + \nabla p = \rho \mathbf{g} \tag{2}$$

$$\rho C_p \left(\frac{\partial T}{\partial t} + \mathbf{v} \cdot \nabla T \right) - k\nabla^2 T = 0, \tag{3}$$

where $\mathbf{v}$ is the velocity, η the viscosity, $\dot{\varepsilon}$ the strain rate tensor, p the pressure, ρ the density, $\mathbf{g}$ the gravitational acceleration vector, C_p the specific heat capacity, T the temperature and k the thermal conductivity. Specific values for the parameters defined in this section can be found in Table 1.

Our models include three compositional fields that are rheologically distinct from the background material (but have equivalent density). We track and conserve these compositional fields (eq. 4) using the fields method (Bangerth *et al.* 2019).

$$\frac{\partial C_i}{\partial t} + \mathbf{v} \cdot \nabla C_i = 0. \tag{4}$$

Here, i identifies each individual composition ($i = 1, 2, 3$).

2.2 Model setup

We consider dynamic intra-oceanic subduction: both the overriding and subducting plates are oceanic, and our system evolves self-consistently for 50 Myr. We vary the width of the plates between 2000 and 1000 km, and trench mobility is taken into account by fixing either the upper or the lower plate, or by leaving them both free to move. The model domain is a box $(x, y, z) = (4500, 1800, 900)$ km, where x is the length, y the width and z the depth (Fig. 1). We take advantage of plate symmetry about the centre of the subduction system (i.e. the trench-perpendicular vertical axis at $y = 0$), which enables us to run models with half of the stated plate widths. Our reference model corresponds to a case in which both plates are free to move and their full plate width is 2000 km. Our models include the first 240 km of the stronger lower mantle (*cf.* Stegman *et al.* 2006), to better simulate the interaction between the slab and the 660 km depth discontinuity. The initial setup does not include lateral plates, but relatively thin plates form during the model run due to surface cooling and the formation of a stiff thermal boundary layer. This counterbalances in part the significant along-strike deformation of the active plates that would occur if lateral plates were completely omitted (Yamato *et al.* 2009). All model boundaries are mechanically free slip.

The temperature is set to $Ts = 0$ °C at the surface, and the other boundaries are fixed at the mantle potential temperature $T_m = 1421.5$°C (GDH1 plate cooling model: Stein & Stein 1992). The initial thermal structure of the oceanic plates are half-space cooling

Table 1. List of parameters with values and units.

Parameter	Symbol	Value	Unit
Reference values			
Reference viscosity	η_{ref}	2.5×10^{20}	Pa · s
Reference strain rate	$\dot{\varepsilon}$	5×10^{-15}	s^{-1}
Reference density	ρ_0	3300	kg m^{-3}
Gravitational acceleration	**g**	9.81	m s^{-2}
Specific heat capacity	C_p	940	J K^{-1}
Surface temperature	T_s	0	°C
Mantle potential temperature	Tm	1421	°C
Adiabatic gradient		0.3	° km^{-1}
Thermal conductivity	k	3	W m^{-1} K^{-1}
Thermal diffusivity	κ	10^{-6}	m^2 s^{-1}
Thermal expansivity	α	3×10^{-5}	K^{-1}
Rheology: Diffusion and dislocation creep			
Prefactors	A_{diff}	Uper mantle diffusion: 1.92×10^{-11}	$Pa^{-1}s^{-1}$
		Lower mantle diffusion: 1.67×10^{-13}	$Pa^{-1}s^{-1}$
	A_{disl}	Upper mantle dislocation: 5.858×10^{-18}	$Pa^{-n}s^{-1}$
Exponent	n	Dislocation: 3.5	-
Activation volumes	$V_{a,\text{ diff}}$	Upper mantle diffusion: 4×10^{-6}	m^3
		Lower mantle diffusion: 2.5×10^{-6}	m^3 mol^{-1}
	$V_{a,\text{ disl}}$	Upper mantle dislocation: 12×10^{-6}	m^3 mol^{-1}
Activation energies	$E_{a,\text{ diff}}$	Diffusion: 300×10^3	J
	$E_{a,\text{ disl}}$	Dislocation: 540×10^3	J
Gas constant	R	8.3145	J mol^{-1} K^{-1}
Rheology: Pseudo-plastic yielding			
Friction coefficient	a	0.6	-
Cohesion	b	60	MPa
Prefactor	λ	0.1	-

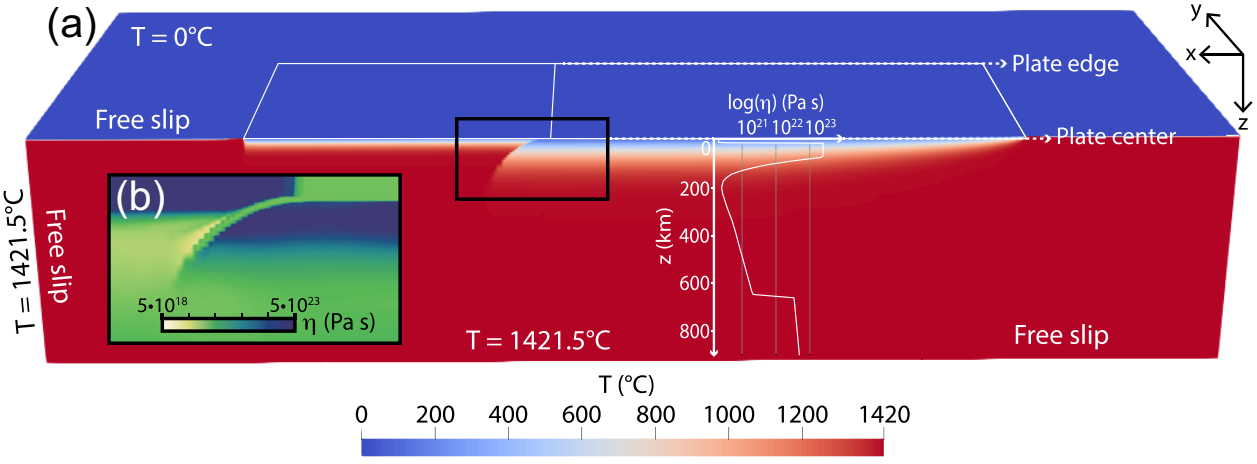

Figure 1. (a) Initial thermal structure for the reference model (with free plates and a 2000 km plate width). (b) The initial viscosity field within the plate interface area. The weak material on top of the subducting plate corresponds to the crustal layer. In panel (a), we also include a depth profile of the model viscosity.

profiles (Turcotte & Schubert 2002) for subducting plate and overriding plate ages of 90 and 10 Myr, respectively (see Table 1 for thermal parameter values). Our subduction models are incompressible but we add a 0.3 °C km^{-1} adiabatic temperature gradient to the extracted slab top temperatures (*cf.* van Keken *et al.* 2011). A weak (2×10^{20} Pa · s) and thin (10 km thick) crust, with the same density as the mantle, is embedded into the top of the subducting plate to decouple the upper and lower plates (e.g. Běhounková & Čížková 2008; Capitanio *et al.* 2010; Quinquis *et al.* 2011). Subduction is initiated by extending the weak crust and subducting plate thermal anomaly to a depth of ≈120 km and with a radius of curvature of 250 km. When juxtaposed next to the thinner (and hence lighter) overriding plate, this provides the initial density anomaly needed to drive subduction. Model densities are exclusively temperature dependent and computed relative to the reference density, $\rho_0 = 3300\,\text{kg m}^{-3}$, of material at the mantle potential temperature: $\rho = \rho_0[1 - \alpha(T - T_m)]$.

In addition to the background material, the model subduction zone contains three additional compositions: the crust, a rheologically stronger material that makes up both the overriding plate and

a 15-km-thick core in the middle of the subducting plate, and weak boxes at the end of each of the free plates. All three are characterized by different rheologies or viscosities (see Section 2.3), but have equivalent densities to the background material. The weak boxes, which are 50 km wide and 50 km deep, assist with maintaining ridge-like thermal structures at the end of each of the free plates. These three components are implemented as different compositional fields, and tracked by solving eq. (4).

An important property of our model is the depth of decoupling (or decoupling depth, DD, determined by computing the depth at which a viscosity contour for $\eta = 10^{21.5}$ Pa · s intersects the slab top), which marks the downdip beginning of viscous coupling between the slab-top and the hot and circulating mantle wedge (Furukawa 1993). At this depth, the slab transitions from being overlain by cold (and stiff) forearc material to being overlain by warm (and weak) mantle material; this depth is, therefore, also associated with a relatively abrupt downdip increase in slab-top temperature. At current Earth subduction zones, which mainly correspond to mature phases of subduction, the DD has been estimated by constraining kinematically driven thermal models with surface heat flow measurements and, following this, hypothesized to be at 60–80 km depth (Furukawa 1993; Wada & Wang 2009). In our models, we allow the DD to vary with time as a function of evolving subduction zone properties, but limit it at an imposed maximum decoupling depth (MDD) of 100 km (where we convert the weak oceanic crust to an equivalent strength as the surrounding mantle and hence prohibit slab-mantle coupling beyond this depth). In reality, this MDD is likely associated with a down-dip transition from weak hydrous minerals to stronger anhydrous minerals (e.g. Wada *et al.* 2008; Hirauchi & Katayama 2013; Agard *et al.* 2020; Peacock & Wang 2021); here, we simplify this by pinning it to a constant depth. The initial DD, corresponding to the depth at which the base of the overriding plate is in contact with the slab-top, is ≈30 km: this corresponds to the initial thermal thickness of the 10 Myr old overriding plate. As the model evolves, the DD gradually deepens in a self-consistent manner, in some cases all the way to the imposed MDD limit. This DD increase, from subduction initiation to maturity, is in agreement with inferences from previous modelling and observational studies (e.g. Agard *et al.* 2020; Holt & Condit 2021; Wang *et al.* 2023).

2.3 Rheology

The mantle has a composite diffusion–dislocation creep rheology. The diffusion and dislocation creep flow laws are given by eqs (5) and (6):

$$\eta_{\text{diff}} = \frac{1}{A_{\text{diff}}} \exp\left(\frac{E_{\text{diff}} + pV_{\text{diff}}}{RT}\right) \tag{5}$$

$$\eta_{\text{disl}} = A_{\text{disl}}^{\frac{-1}{n}} \dot{\varepsilon}_{\text{II}}^{\frac{1-n}{n}} \exp\left(\frac{E_{\text{disl}} + pV_{\text{disl}}}{nRT}\right) \tag{6}$$

where $A_{\text{diff/disl}}$ are the pre-factors for diffusion and dislocation creep, n the dislocation creep power-law exponent, $\dot{\varepsilon}_{\text{II}}$ is the second invariant of the strain rate, $E_{\text{diff/disl}}$ the activation energy, $V_{\text{diff/disl}}$ the activation volume, R the gas constant and T the temperature, which includes the prescribed adiabatic gradient of 0.3 ° km^{-1}. The values for these parameters, reported in Table 1, are in accordance with experimental values for dry olivine (Hirth & Kohlstedt 2003). We compute the prefactors $A_{\text{diff/disl}}$ for upper mantle diffusion and dislocation creep such that, at a depth of 330 km and reference strain rate of 10^{-15} s^{-1}, each component has a reference value $\eta_{\text{diff}} = \eta_{\text{disl}} = 4 \times 10^{20}$ Pa · s. When averaged together, this produces a reference upper mantle viscosity of 2×10^{20} Pa · s. The lower mantle is more viscous and is set to only deform via diffusion creep. The upper to lower mantle viscosity jump is parametrized with a diffusion creep viscosity that is equal to 15 times that of diffusion creep in the lowermost upper mantle. Due to the operation of dislocation creep in the upper mantle, the effective viscosity jump is actually ≈30, as is compatible with geoid constraints (e.g. Hager 1984).

Throughout the domain, the effective viscosity is then computed by combining these viscosity components with η_{yield} via a harmonic mean:

$$\eta = \left(\frac{1}{\eta_{\text{diff}}} + \frac{1}{\eta_{\text{disl}}} + \frac{1}{\eta_{\text{yield}}}\right)^{-1}. \tag{7}$$

where η_{yield} is is a plastic 'viscosity', which is incorporated to loosely mimic the large-scale weakening effects of brittle faulting at lithospheric depths. This plastic deformation only operates within the lithosphere; at high stresses, η_{yield} reduces to cap the model stress at the prescribed yield stress, τ_{yield}. η_{yield} is therefore calculated as:

$$\eta_{\text{yield}} = \frac{\min\left(\tau_{\text{yield}}, 0.5\text{ GPa}\right)}{2\dot{\varepsilon}}, \tag{8}$$

where the yield stress τ_{yield} is approximated by a Coulomb friction criterion for optimally oriented faults:

$$\tau_{\text{yield}} = (a\sigma_n + b)\,\lambda, \tag{9}$$

where $a = 0.6$ is the friction coefficient, $b = 60$ MPa is the cohesion, σ_n is the lithostatic pressure and $\lambda = 0.1$ is a constant slab weakening pre-factor. These values are broadly consistent with previous dynamic subduction modelling studies (e.g. Enns *et al.* 2005; Di Giuseppe *et al.* 2008; Holt *et al.* 2015; Behr *et al.* 2022). The weak boxes that we add at the edges of the free plates (to decouple them from the adjacent, stiff material of the growing thermal boundary layer) are implemented by reducing the yield stress pre-factor ($\lambda = 0.05$). The overriding plate and the core in the subducting lithosphere are made strong by switching off yielding in these regions. The viscosity is limited between minimum and maximum values of 2.5×10^{18} and 2.5×10^{23} Pa · s.

2.4 Numerical methods

The ASPECT finite element code includes adaptive mesh refinement (AMR) functionality. In our models, we refine the mesh as a function of viscosity, temperature, and composition: greater refinement occurs in areas where the gradients of these properties are large. This AMR setup produces highly refined areas along the evolving plate interface and within the slab, and a coarser mesh in regions without high viscosity, temperature, or compositional gradients (e.g. the lower mantle). In these latter regions, cubic finite elements are 56 km wide/thick, while in highly refined regions, we reach a maximum resolution of 1.8 km. In addition to this AMR, we fix the upper 100 km of the model domain, and the upper-lower mantle boundary region, to have a minimum resolution of 7 km.

To verify our solver tolerances are sufficiently strict and our model resolution is sufficiently high, we performed numerical accuracy and resolution tests on a 2-D version of our reference model. Relative to the reference setup, we reduced (i) the linear (from 10^{-3} to 10^{-4}) and non-linear (from 5×10^{-3} to 5×10^{-4}) solver tolerances and (ii) doubled the mesh resolution. We test these changes by comparing the convergence rate evolution. Adjusting the solver tolerances has no discernible impact (Fig. S1a). Doubling the resolution does not alter the overall trend, but results in minor convergence rate differences that are <5 per cent for most of the run (Fig. S1b).

3 RESULTS

We focus on key aspects of subduction dynamics and their effect on the spatio-temporal evolution of slab-top temperature. In particular, the mantle wedge flow regime, convergence rate and DD, all of which significantly impact slab temperatures. In order to generate wide variability in such properties, we examine models with variable plate mobilities (both plates free, fixed subducting plate, fixed overriding plate) and variable plate/slab widths (1000 km width, 2000 km width and infinite width/2-D models). Fixing the subducting or overriding plate results in, respectively, enhanced or reduced slab rollback (e.g. Enns *et al.* 2005; Capitanio *et al.* 2010; Holt *et al.* 2015). Slab rollback is also affected by plate width, with narrow subduction zones previously associated with faster rollback, more toroidal flow, and higher along-strike gradients in subduction properties (Piromallo *et al.* 2006; Stegman *et al.* 2006).

3.1 Reference case

Our reference model contains 2000 km wide plates and free subducting and overriding plates. The temporal evolution of the slab shape and slab-top temperature is shown in Fig. 2(a).

We identify three main stages of subduction by focusing on time periods with distinct convergence rates (Figs 3a and b). In our analysis, we do not consider thermal structure during the slow subduction initiation phase that occurs during the first ≈5 Myr. This is to avoid aspects of thermal structure that are inherited from the initial conditions. In the rest of the paper, we therefore refer to the three subsequent subduction stages: (i) *free sinking* of the slab through the upper mantle: After subduction initiation, the slab sinks rapidly through the upper mantle. The convergence rate at the centre of the plate is ≈8 cm yr^{-1} at the plate centre and ≈7 cm yr^{-1} at the plate edge; (ii) *interaction with the lower mantle*: As the slab impinges on the more viscous lower mantle (≈15 Myr into the model run), it bends backwards on top of the viscosity discontinuity. The convergence rate decreases rapidly, until it reaches ≈5 cm yr^{-1} at the plate centre and ≈4 cm yr^{-1} at the edge and (iii) *mature subduction*: subduction slows down as the slab continues to flatten on the upper-lower mantle boundary. The convergence rate reaches a minimum of ≈2 cm yr^{-1} at the plate centre and ≈1 cm yr^{-1} at the edge.

This reference model is characterized by slab rollback (20–70 per cent of the convergence rate depending on the subduction phase) and, as described, a higher convergence rate at the plate centre than the edge (Figs 3a and b). Roll-back induced toroidal flow around the slab edges, from regions of relatively high to relatively low pressure, also enables the trench to deform along-strike (e.g. Funiciello *et al.* 2003; Schellart 2004; Piromallo *et al.* 2006). After initiating at an equivalent depth, the DD becomes deeper at the plate edge than at the centre, by 5 km after ≈ 50 Myr (Figs 3c and d).

We extract slab-top *P–T* conditions at the plate centre and plate edge, for times within the three characteristic subduction phases, to probe along-strike temperature variation. To avoid the highly deformed area at the very edge of the plate, we extract edge temperatures at a fixed lateral position corresponding to 50 km (in the along-strike direction) from the location of the plate edge at 14 Myr. Despite minor amounts of trench-parallel plate/slab shortening, this distance enables us to always be extract temperatures from within the slab and not the adjacent, flowing mantle. The only exception is the 45 Myr profile for the fixed subducting plate case; intense trench-parallel deformation requires that we extract edge temperatures at ∼50 km from plate edge at this specific time, in order to have comparable results to the other models/times. The P-T conditions are extracted along the upper surface of the compositional crust (i.e. the upper layer of the slab). As time progresses, the slab-top cools for depths ≪200 km (Figs 4a and S2). At depths of ≥200 km, cooling is negligible and the near-constant temperature is ≈850 °C. At a given time, slab temperature increases rapidly down to a depth of 50–100 km. At this depth, a kink, most visible for earlier times and located between pressure values of 2– GPa (Fig. 4), is present in the *P–T* conditions, which corresponds to a rapid increase in temperature centred on the time-evolving DD (*cf.* Wada & Wang 2009; Syracuse *et al.* 2010).

Slab-top thermal conditions exhibit along-strike variability. To illustrate this, we compute the difference in temperature between plate centre and edge for each model, at the same times and three different depths (Fig. 4b): 60 km, corresponding to the temperature at or above the DD (depending on the evolving depth of the DD at the particular time), and 130 km and 200 km, corresponding to two depths greater than the DD in which we have viscous coupling between the slab-top and mantle wedge. The absolute temperature difference varies between 5 and 25 °C. In general, the slab edge is warmer than the centre of the slab during the first two phases of subduction by ≈10 °C. During the final, mature phase of subduction, this trend reverses as the slab centre becomes warmer than the slab edge by 10–25 °C.

3.2 Variable plate mobility

Our reference case consists of two plates that are free to move horizontally (i.e. are not pinned to the model sidewalls). Fixing one of the plates strongly influences trench/slab mobility which, in turn, exerts a significant control on slab evolution and the associated mantle flow (*cf.* Christensen 1996; Stegman *et al.* 2010). Here, we assess the impact of this variability on along-strike temperature variations.

We first describe the slab dynamics. Regardless of plate mobility, these models have similarities with the free plates reference case: Convergence rate is again lower at the plate edge than at the centre (Figs 3a and b) and undergoes a similar pattern of evolution through the three subduction phases. The DD is again deeper at the plate edge than the centre (Figs 3c and d) and the DD difference, between the edge and centre, increases as the model evolves.

There are, however, key differences with respect to the free plates reference. Most notably trench retreat (Figs 3a and b): In the fixed overriding plate case, trench retreat is negligible (<1 cm yr^{-1} at all times) and, as a result, so is along-strike trench deformation. In the fixed subducting plate case, trench retreat is more rapid than in the reference case throughout the whole subduction process, typically by 20–50 per cent, which enhances trench curvature. Convergence rate also varies with plate mobility (Figs 3a and b): In the fixed overriding plate case, it is up to 60 per cent lower than in the reference case. In the fixed subducting plate case, the convergence rate is again lower than in the reference case for early subduction, but it with similar values during the mature phases. The DD is, in general, greater in the fixed overriding plate case than the free plates reference, by ≈10 km, but the fixed subducting plate case has similar DD values. Similarly, the centre-to-edge DD increase is greater in the fixed overriding plate case, reaching ≈15 km during mature subduction, but this increase is significantly reduced in the the fixed subducting plate case (to 2–3 km of along-strike variation).

Both of the new cases exhibit similar trends regarding slab-top *P–T* evolution and its variation along-strike. Fig. 4 shows that, as in the reference, the slab-top temperature decreases with time, increases

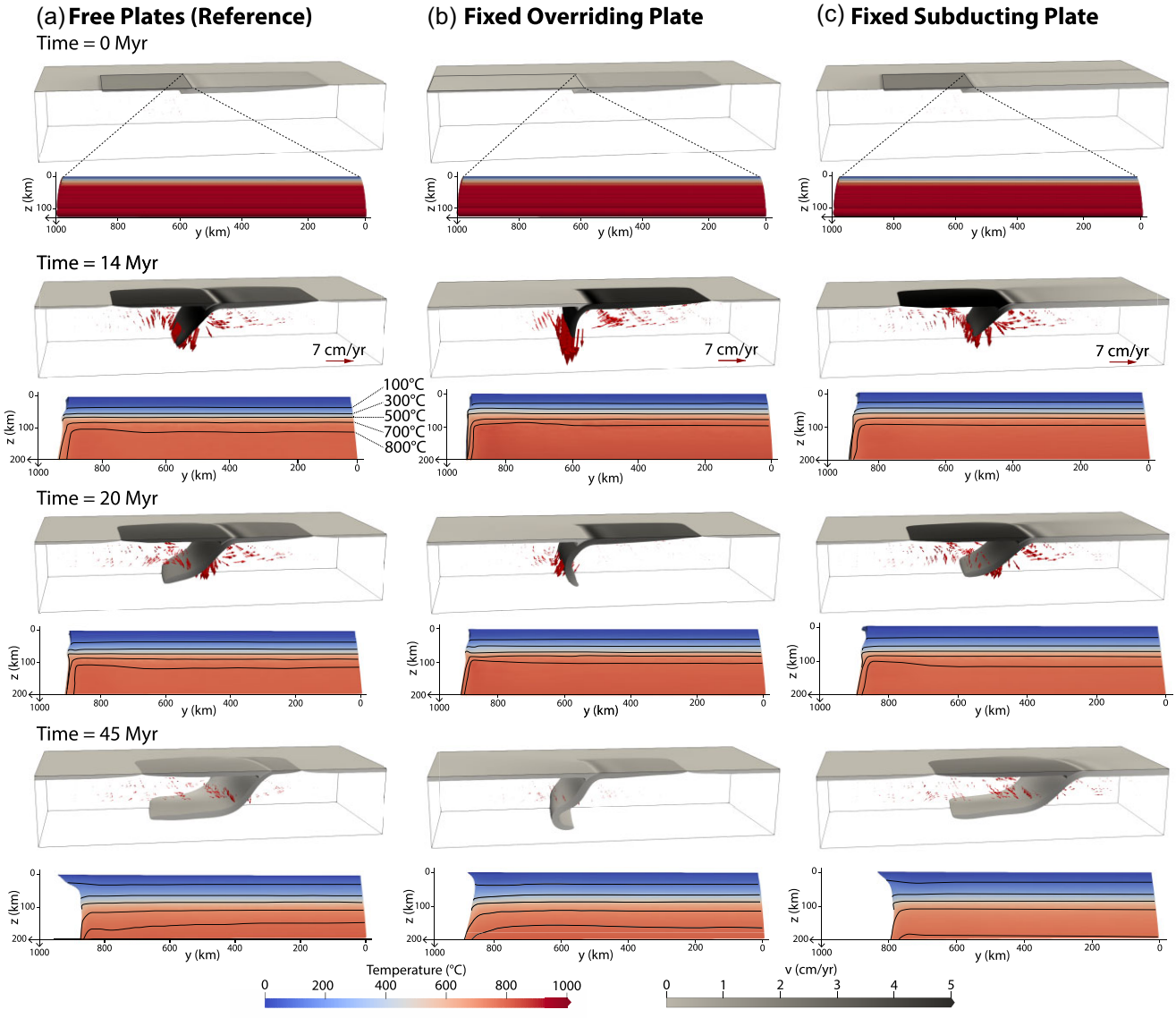

Figure 2. Temporal evolution of models with variable plate mobilities, each with a 2000 km plate width (i.e. 'wide' plate models). For each time-step, we show the slab shape, upper mantle velocity field and the slab-top temperature distribution to a depth of 200 km (with the exception of and$t = 0$ Myr, where the slab-top reaches a depth of only 120 km). The black lines show isotherms at 100, 300, 500, 700 and 800°C. (a) corresponds to the reference model depicted in Fig. 1; (b) corresponds to the wide, fixed overriding plate model and (c) corresponds to the wide, fixed subducting plate model. The grey outline in the top row shows initial the position of the overriding plate.

with depth and exhibits a kink in all cases. There is also the same sense of along-strike variability: The edge of the plate is warmer than the centre during the early stages of subduction and colder for mature subduction. While the same trends persist, there are variations in the magnitudes of along-strike slab-top temperature changes. In the fixed overriding plate case, the absolute temperature difference varies between 5 and 30 °C, while for the fixed subducting plate case it varies between 5 and 50 °C. This is relative to less variability in the free plates reference (5–25 °C).

3.3 Variable plate width

We now vary the plate/slab width for both the free plates and fixed overriding plate cases, to examine the effects of three-dimensionality in more detail. We reduce the plate width to examine a narrower subduction zone (1000 km plate width) relative to the reference (2000 km width).

For both cases, the first-order evolution is broadly consistent. As for the wider plate cases, convergence rate remains higher at the plate centre than at the edge (Figs 5a–d) and the DD is greater at the plate edge than the plate centre (Figs 5e and f). Fig. 6 compiles the DD variation in all models with variable plate widths (i.e. the free plates and fixed overriding plate cases); the plate centre always has the shallower DD. Vigorous toroidal flow occurs in both free plate cases (Fig. S3), as both slabs exhibit significant rollback, but is negligible in both fixed overriding plate cases (Fig. S4). The two clearest differences relate to the convergence rate and DD: Convergence rate is lower in the narrower plate models, the DD is generally deeper, and the magnitude of the along-strike (centre-to-edge) DD increase is reduced.

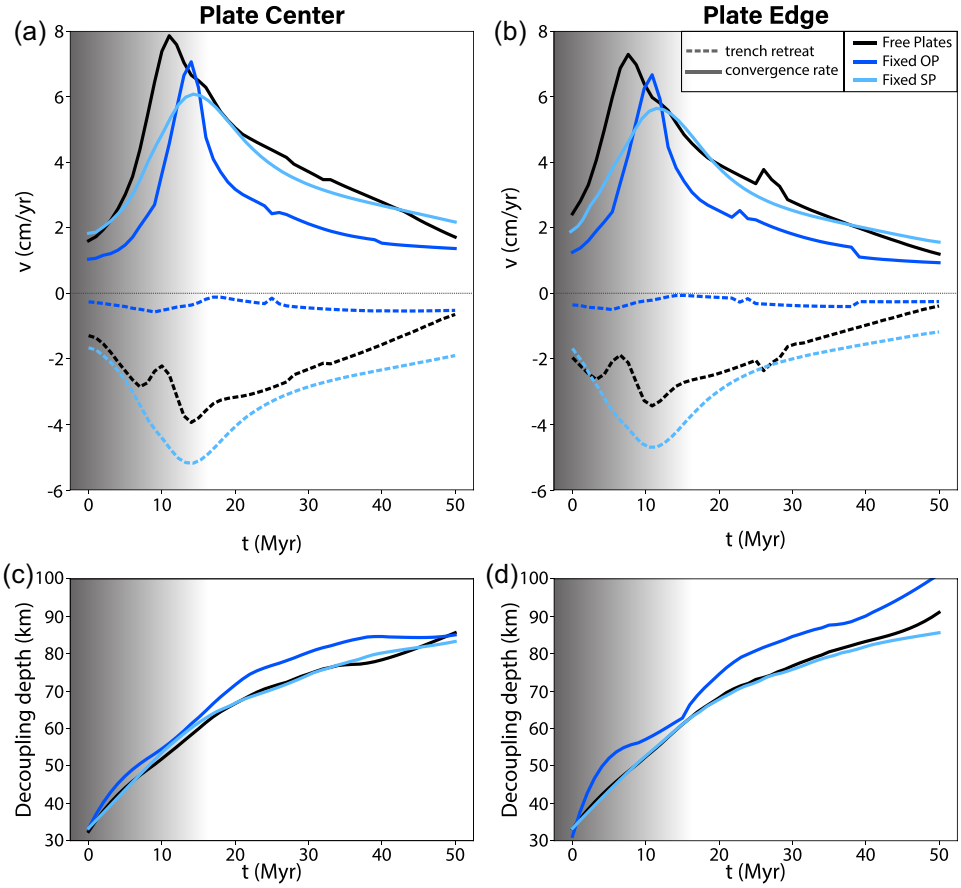

Figure 3. (a, b) Surface kinematics and (c, d) decoupling depth evolution for models with variable plate mobilities, each with a 2000 km plate width. Velocities and decoupling depths are extracted from both the centre and edge of the model subduction zones (see Fig. 1 for locations). Solid lines and dashed lines correspond to convergence and trench migration rates (negative = trench retreat), respectively. The black lines represents the free plates (reference) case and the shades of blue from dark to light represent, in order, the fixed overriding plate and fixed subducting plate cases. The shaded area indicates the subduction initiation and free sinking phases within the free plates reference model.

In both narrow subduction zone cases, the *P–T* conditions again exhibit a decrease in temperature with time (Fig. 7a) and along-strike temperature differences (Fig. 7b), both following the same trend as the reference model. However, at 20 Myr, the narrow, free plates model exhibits negligible temperature difference along-strike, while for the other two times, the absolute temperature difference is greater than within the reference model (a maximum of ≈32 °C relative to ≈25 °C in the reference). The narrow, fixed overriding plate case exhibits a greater temperature difference at 20 Myr (≈30 °C maximum) with respect to the equivalent wide plate case (≈15 °C maximum), while during the earliest phase, at 14 Myr, this trend is reversed.

3.4 Comparison with 2-D cases

To extend the plate width exploration, we constructed equivalent 2-D models for the fixed and free overriding plate cases. 2-D subduction models are equivalent to infinitely long trenches; these tests thus enable us to further isolate the effect of the third dimension. In the free plates model, the 2-D convergence rate is higher (≈10 per cent) than that extracted from the centre of the 3-D case until the slab starts interacting with the lower mantle; after which, it becomes significantly lower (Figs S5a and c). The DD is deeper than within the equivalent 3-D model (both at the centre and edge of the 3-D slab). In the fixed overriding plate case, both the convergence rate and DD are similar to the 3-D model (Figs S5b and d).

We compute the temperature difference between slab-tops in the 2-D and 3-D cases; in the 3-D case, we use the slab-top temperature extracted from the plate centre (Fig. 8). The overall trend is independent of overriding plate mobility: for early stages and shallow depths (60 km), the slab-top is warmer in the 3-D models by 9–25 °C. For all other times and depths, the 2-D slab-top is warmer by 7–35 °C.

4 DISCUSSION

Our models highlight an along-strike gradient in slab-top temperature that evolves through time. We start by addressing our modelled subduction zone evolution—particularly the convergence rate, decoupling depth (DD), and mantle flow field—and show how these quantities combine to dictate the slab-top thermal evolution. We then compare our modelling results to previous modelling studies and natural observations.

4.1 Slab dynamics

The temporal evolution of our reference model, with free and 2000-km-wide plates, is characterized by slab rollback, vigorous toroidal

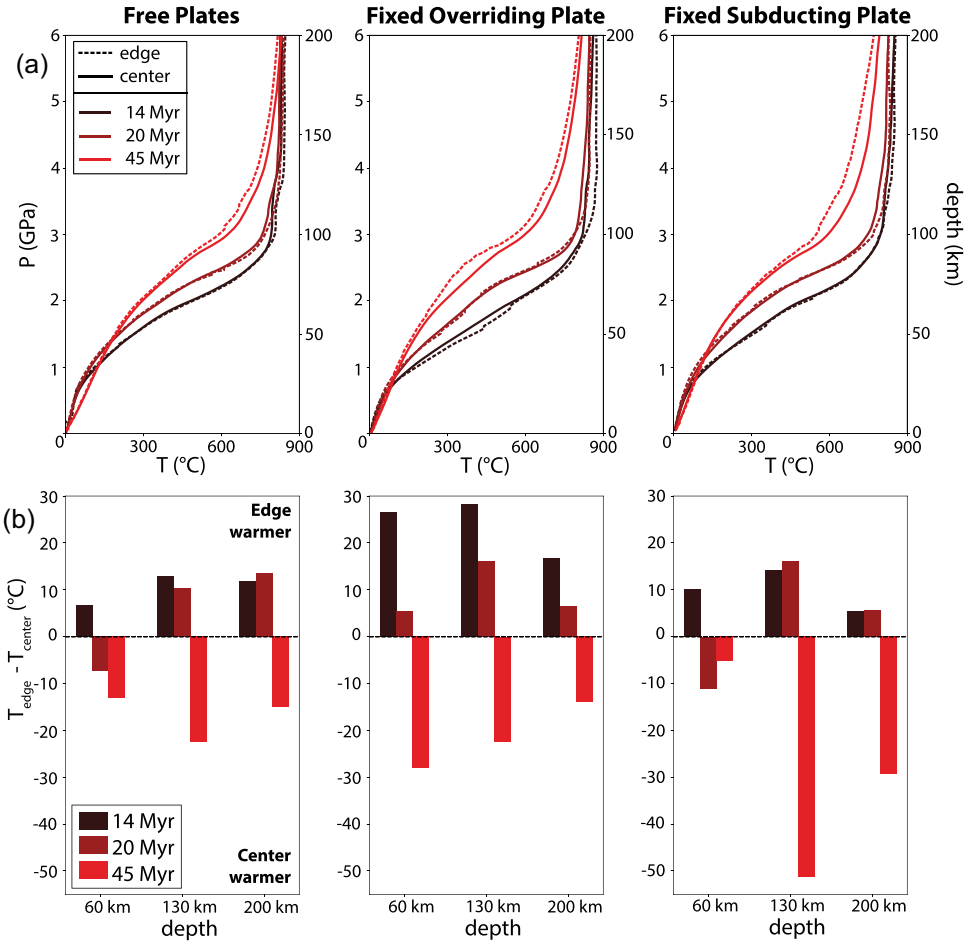

Figure 4. (a) Slab-top pressure–temperature (*P*–*T*) conditions for models with variable plate mobilities, each with a 2000 km plate width, and (b) the associated slab-top temperature difference between the slab at the edge and centre of the subduction zone at 60, 130 and 200 km depths. In panel (a), dashed lines denote the plate edge *P*–*T* conditions and the solid lines the plate centre conditions. In panel (b), the different shades of red indicate the three distinct times.

flow at depth and along-strike variability in trench retreat and convergence rates. The convergence rate is greater at the plate centre than the plate edge, by ≈10 per cent, which strongly affects the DD. As the model progresses, the DD tends to deepen due to the thermal ageing of the overriding plate and the associated development of a cold forearc wedge corner. On the other hand, a higher convergence rate increases the vigour of poloidal flow generated by slab sinking (Sleep & Toksöz 1971), which, in turn, produces more efficient transport of hot mantle material into the wedge corner. Since the DD marks the transition from the cold forearc nose to the warm mantle wedge, this vigorous transport pushes the DD towards the surface (*cf.* Arcay *et al.* 2007), counteracting the effect of thermal cooling to some extent. At the plate centre, where convergence rates are greater, the DD is therefore shallower than at the plate edge in all of the models. The edge-to-centre DD difference increases with time, and reaches up to 15 km at the end of the run (Fig. 6). As this edge-to-centre DD difference increases with time, so does the average DD, from 30 km at the start to ≈90 km at the end of the model (*cf.* Holt & Condit 2021). Surface heat flux measurements suggest an average DD of 60–80 km at present-day subduction zones (Furukawa 1993; Wada & Wang 2009), and recent geodetic measurements in Honshu, Japan suggest that the DD can indeed vary along-strike by ≈25 km (Dhar *et al.* 2022). This gives us confidence in the natural applicability of the first-order features of our DD evolution and the associated thermal effects (Sections 3.1–3.3). We note that we set the DD limit, or 'maximum decoupling depth (MDD)', by the 100 km depth at which we eliminate our weak crust and thereby couple the slab to mantle wedge. In reality, the MDD is likely dictated by a switch from rheologically weak hydrated to stronger anhydrous rocks in either the crust or mantle wedge (Hirauchi & Katayama 2013; Agard *et al.* 2020; Peacock & Wang 2021; Kerswell *et al.* 2021).

Fixing the overriding plate reduces slab rollback/trench retreat (e.g. Capitanio *et al.* 2010; Schellart & Moresi 2013; Holt *et al.* 2015). This results in almost no along-strike trench deformation, negligible toroidal flow, and greater dips by up to 15°. Conversely, fixing the subducting plate promotes elevated slab rollback, more vigorous toroidal flow, and reduces dips by ≈10°. Relative to the reference, convergence rate is lower in the fixed overriding plate case, by up to 2 cm yr^{-1}, which results in a greater DD. Importantly, in all models, the convergence rate is higher at the plate centre than at the edge; this produces the observed DD increase from plate centre to edge.

Varying the plate width does not modify the first-order slab dynamics or the relationship between convergence rate and DD. Reducing the plate width lowers the average convergence rate (Stegman *et al.* 2010) and, in turn, deepens the DD. The most significant effect of increasing the effective plate width (i.e. 2-D

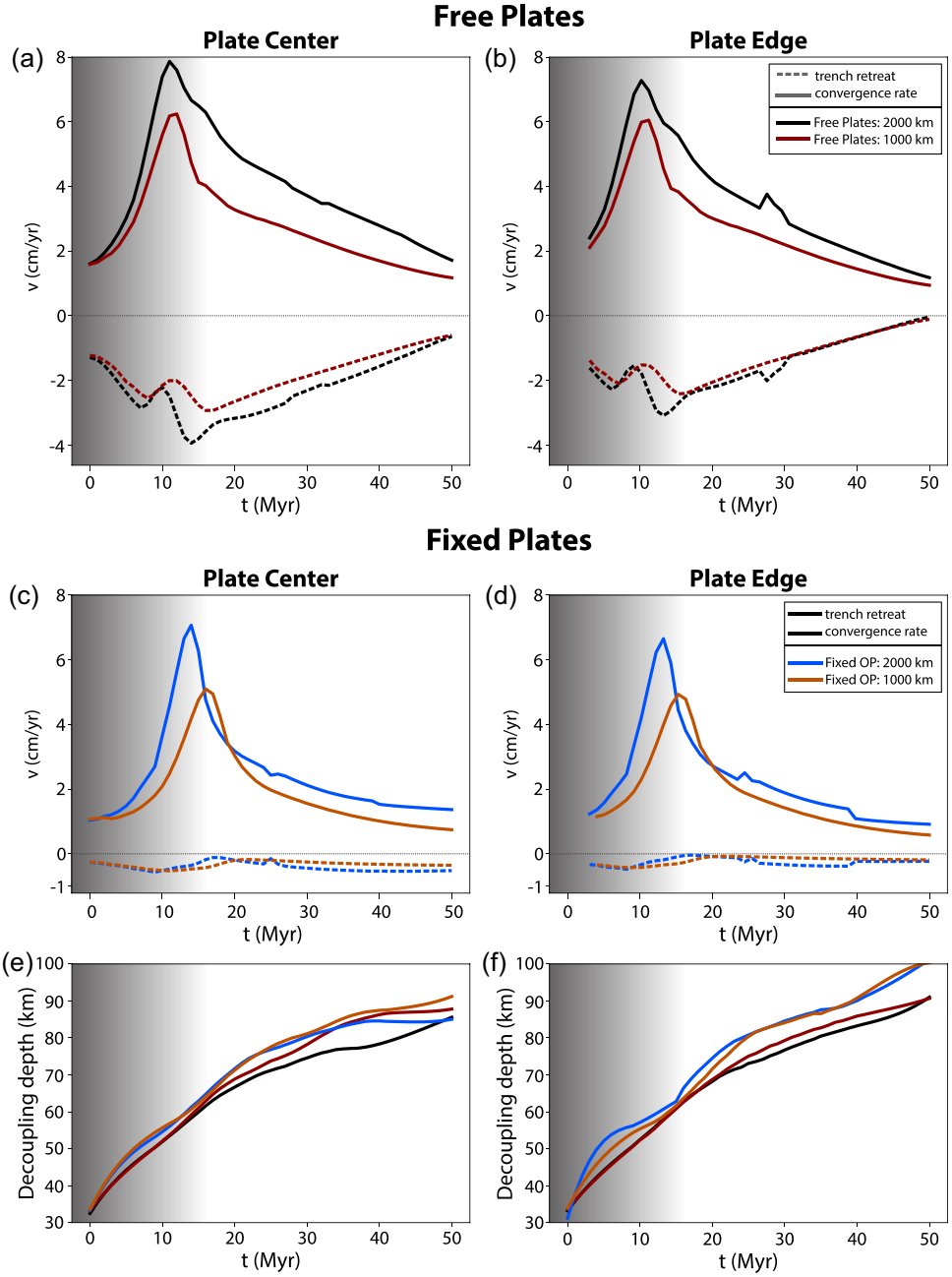

Figure 5. (a–d) Surface kinematics and (e, f) decoupling depth variation for models with variable plate widths, with properties extracted from both the plate centre and the plate edge. In panels (a)–(d), solid lines correspond to convergence rate and dashed to trench motion (negative = trench retreat). Dark and light brown lines correspond to correspond to 1000 km wide free plates and fixed overriding plate cases, respectively. Black and blue lines correspond to correspond to 2000 km wide free plates and fixed overriding plate cases, respectively. The shaded area corresponds to subduction initiation and free sinking for free overriding plates. This phase lasts longer for the fixed overriding plate cases.

models/infinite plate) occurs during mature subduction (i.e. after slab interaction with 660 km) in the free plates model. During this phase, the 2-D convergence rate is reduced relative to the equivalent 3-D case; as expected, this results in an increased DD.

4.2 Spatio-temporal thermal variability

In our models, spatio-temporal variability in convergence rate is the main control on along-strike slab-top temperature variation. The product of convergence rate and plate age (and sometimes the sine of slab dip) is termed the 'thermal parameter' (Kirby *et al.* 1996) and often used as an approximate indicator of slab-top temperatures in models (e.g. van Keken *et al.* 2011) and natural subduction zones (e.g. Wiens 2001). High values, for example due to rapid convergence rates, correspond to cold slabs. Maunder *et al.* (2019) explored how well the thermal parameter predicts slab temperatures within models with different DDs. Because the DD dictates the downdip extent of cold material that blankets the slab, they found that a deeper DD exerts a strong slab cooling effect (*cf.* Wada *et al.* 2008) and hence proposed the DD should be incorporated into

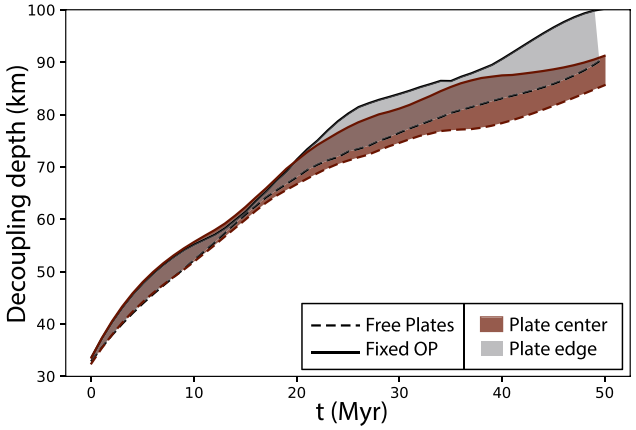

Figure 6. Range of decoupling depths (DD) for all 3-D models with variable plate widths (i.e. free plates and fixed overriding plates cases for 1000 and 2000 km wide plates). The dashed line corresponds to a free overriding plate model (2000 km wide plates case), which has the minimum DDs, and the solid line to a fixed overriding plate model (1000 km wide plate case), which has the maximum DDs. The range of plate edge DDs is in grey and the range of plate centre DDs are in brown. Slabs at the plate edge always have a greater DD than at the centre.

updated formulations of the thermal parameter. This new description is well suited to characterizing the slab-top temperatures in our 3-D models which, as described in previous sections, exhibit significant spatio-temporal variability in not only convergence rate but also the DD. In our dynamic models, the DD is controlled by both the gradual cooling of the overriding plate (i.e. a gradual deepening of the DD) and variability in convergence rate (i.e. a greater rate produces more vigorous mantle flow that resists this deepening of the DD).

In addition to controlling temperature via the rate of slab sinking—as expressed by the classical thermal parameter—this link between convergence rate and DD results in additional along-strike variability in slab-top temperature. These two mechanisms dominate at different stages of subduction and produce the following evolution in along-strike slab-top temperature variation (Fig. 9).

4.2.1 Early stages

During the initial phases of subduction (up to 20 Myr), the convergence rate is high (up to 8 cm yr^{-1} during free sinking) and reaches the maximum value at the slab centre, regardless of plate width and mobility. Following the classical thermal parameter, a higher convergence rate at the slab centre corresponds to rapid advection of the cold slab (relative to warming via thermal diffusion) and so reduced temperatures. Hence, the slab is cooler at the plate centre than at the plate edge ($T_{centre} < T_{edge}$) for all models and at all depths.

4.2.2 Mature subduction

After the slab interacts with the lower mantle (at ≈20 Myr), the average convergence rate decreases by up to 70 per cent, but remains higher at the plate centre than at the edge. Because convergence rates are overall much lower, the basic slab sinking effect, as described for the early stages, is overridden by the effect of the DD. At this stage, enough time has elapsed for the DD to be highly variable along-strike (by 5–15 km, depending on the model). This is because, at the plate edge, a lower convergence rate results in less vigorous poloidal flow and hence a greater DD relative to the plate centre (where more vigorous flow resists deepening of the DD). Thus, as the DD increases at the plate edge, bringing colder isotherms to greater depths, the temperature in this region decreases. The along-strike temperature trend, therefore, reverses: The plate centre becomes warmer than the plate age ($T_{centre} > T_{edge}$). This effect is influential at all of the analysed depths but is generally most pronounced at shallower depths near the DD (i.e. 60 km relative to 130 and 200 km).

The vigor of toroidal flow has been proposed to exert a strong effect on slab temperatures near lateral slab edges. Modelling studies predict toroidal flow concentrated around the slab edges (e.g. Piromallo *et al.* 2006; Jadamec & Billen 2010; Faccenda & Capitanio 2012) and that the associated influx of hot mantle material increases the slab-top temperature (e.g. Kincaid & Griffiths 2003; Kneller & van Keken 2008; Plunder *et al.* 2018). However, in our models, the presence of toroidal flow has a limited effect on slab-top temperature variation: when the overriding plate is fixed and toroidal flow is almost absent (Fig. S6), the general sense and magnitudes of temperature variation are comparable to the free plates reference with substantial toroidal flow. Only when the subducting plate is fixed—and subduction is rollback dominated and toroidal flow is especially vigorous (Fig. S6)—is there a clear signature of toroidal flow-induced heating. During the intermediate phase (20 Myr), the along-strike temperature change is ≈30–50 °C at great depths (130, 200 km); this is elevated relative to the ≈15–25 °C temperature difference in the other two cases with free subducting plates (Fig. 4).

4.3 Comparison with previous modelling studies

In our dynamic models, subduction properties evolve self-consistently with time. Properties that are key with respect to the thermal field include the interlinked velocity field, decoupling depth, and slab shape; their dynamic variability results in a highly time-dependent thermal evolution. Because of this dynamism, it is challenging to compare our results with the kinematically-driven and fixed slab geometry models that are typically used to investigate slab thermal structure. A first-order comparison, however, is useful to place our models in the context of previous work.

Previous kinematically driven modelling studies have shown that a greater DD results in lower slab-top temperatures (Syracuse *et al.* 2010; Perrin *et al.* 2018; Maunder *et al.* 2019; Wang *et al.* 2023). In addition, previous time-dependent 2-D models exhibit a gradual deepening of the DD, due to the conductive cooling of the overriding plate (with mantle wedge flow resisting this DD increase to some extent). Taken together, this causes a gradual cooling of the slab-top from early to mature subduction (Kincaid & Sacks 1997; Holt & Condit 2021; Zhou & Wada 2021). Our 3-D models exhibit the same trend but enable us to probe the time dependency of slab thermal structure in the third (along-strike) dimension. Our key finding is that the plate centre is cooler than the plate edge for early subduction and warmer for mature subduction. Before we compare our modelled along-strike thermal variability with existing 3-D modelling studies, we note that the slab-top temperature difference between our 3-D models (at the plate centre) and equivalent 2-D models is broadly equivalent to the benchmark models of Bengtson & van Keken (2012). Below the DD, slab-tops in our 2-D models are up to 35 °C warmer than the equivalent 3-D case. In Bengtson & van Keken (2012), the equivalent values are ≈50 °C, with the discrepancy likely due to a more curved trench in this previous study.

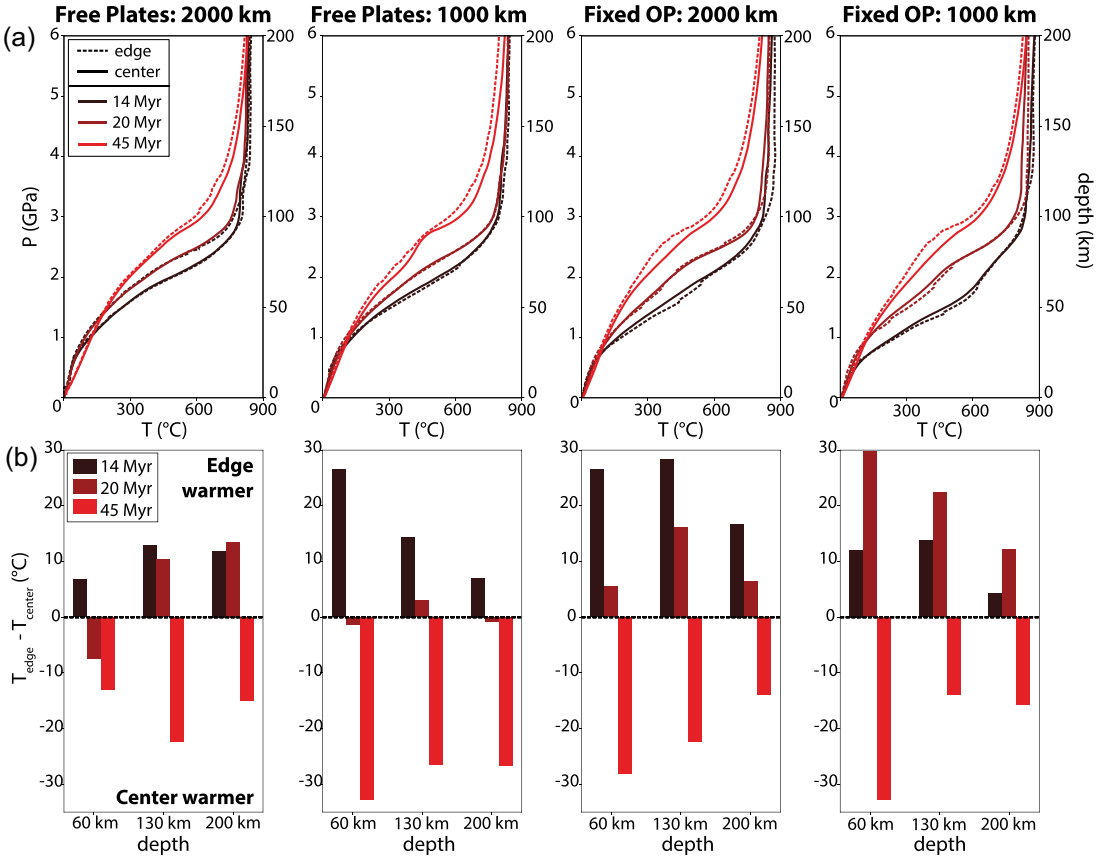

Figure 7. (a) Slab-top *P–T* conditions for models with variable plate widths, and (b) the associated temperature difference between the slab-top at the edge and centre of the subduction zone at 60, 130 and 200 km depths. In panel (a), dashed lines denote the plate edge *P–T* conditions and the solid lines the plate centre paths. In panel (b), different shades of red indicate the three distinct times.

Although our models highlight a new behaviour with regards to slab-top temperature variability—that is a flip in the sense of along-strike thermal variation—the along-strike variation in slab-top temperature (≤50 °C) is on the low end of the range commonly cited in the modelling literature (from 50 to 200 °C; e.g. Bengtson & van Keken 2012; Morishige & van Keken 2014; Ji *et al.* 2016; Plunder *et al.* 2018). In these studies, toroidal flow is invoked as a primary driver of along-strike temperature variation but, in our models, toroidal flow only has a clearly identifiable effect on slab-top temperature at great depths (≥130 km) within the rollback dominated, fixed subducting plate case (Figs 2c, 4 and S6). We suspect that this difference is due to convergence obliquity relative to trench strike (e.g. Wada *et al.* 2015; Ji *et al.* 2016; Plunder *et al.* 2018) and/or high trench curvature (e.g. Bengtson & van Keken 2012) in most of these previous models. Higher obliquity and curvature both drive more vigorous trench parallel flow and hence result in result in greater along-strike temperature differences. In complex tectonic situations, with highly non-linear slab shapes and/or multiple nearby slabs, toroidal or trench parallel flow can be particularly vigorous and hence produce even greater along-strike temperature anomalies (e.g. Araya Vargas *et al.* 2021; Wada *et al.* 2015; Ji *et al.* 2017; Wada & He 2017). Additional tests in some of these studies (e.g. Bengtson & van Keken 2012; Plunder *et al.* 2018), however, consider subduction zones with lower trench curvature and subduction obliquity; this results in less vigorous trench parallel flow and hence smaller temperature variations (e.g. ≈30–50 °C), as is consistent with the ≤50 °C of along-strike slab variability in our models. We also note that these previous models do generally exhibit the same along-strike trend as our models during the mature subduction phase (i.e. the slab-top is warmer at the centre than the edge of the subduction zone).

The analogue models of Kincaid & Griffiths (2003, 2004) are often also used as evidence for the pronounced effect of toroidal flow on slab temperatures. They are most comparable to our mature subduction stage and predict along-strike temperature differences of 35–120 °C and, as in our models during this phase, cooler slab edges if trench retreat is dominant. In these models, a temperature increase at the centre of the slab is attributed to the focusing of toroidal return flow around the slab and into the slab centre. Again, the magnitude of along-strike temperature variation is of the same sign, but generally of greater magnitude than our modelled along-strike temperature variation during mature subduction, which we primarily attribute to along strike DD variations as opposed to toroidal flow. In this case, the discrepancy is not due to oblique subduction or curved trenches as Kincaid & Griffiths (2003, 2004)'s models, like ours, have straight trenches and near-orthogonal convergence. Rather, toroidal flow is again more vigorous in Kincaid & Griffiths models; we suspect this is partially due to their slabs being rigid and hence unable relieve a component of dynamic pressure build-up via slab deformation (*cf.* Kincaid & Olson 1987). Subduction is also entirely rollback driven and the plates are narrower (650 km width), relative to our 1000–2000 km wide plates and 20–70 per cent of convergence accommodated by rollback in our models with free subducting plates. In our models, with wider

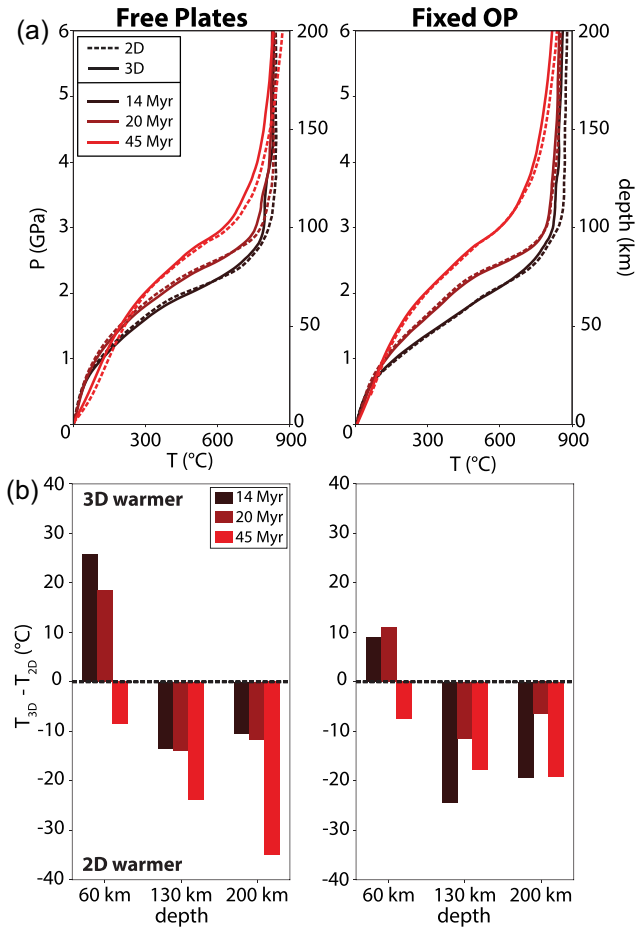

Figure 8. (a) *P–T* conditions for the 2-D versus 3-D cases and (b) slab-top temperature differences between 2-D and 3-D models at 60, 130 and 200 km depths. In (a), the solid line denotes the 3-D case; the dashed lines the 2-D case. The different shades of red indicate the three distinct times.

plates and generally less rollback, less toroidal flow (and hence hot mantle material) reaches the plate centre (Fig. S7), thereby driving less slab-top heating due to this mechanism. However, despite this discrepancy in the magnitude of thermal variability, Kincaid & Griffiths (2003, 2004) also highlight a correlation between lower subduction velocities and a greater DD, and hence cooler slab-top temperatures, as found to be important within our models.

To summarize, our models suggest a relatively limited role for toroidal flow-induced slab heating—and hence reduced along-strike slab-top temperature variation—in tectonic situations where trenches are relatively wide, straight and accommodate near-orthogonal convergence, and where slabs are able to deform. However, when convergence rates are free to evolve in time and along-strike, the sense of variation may be similar to previous modelling studies during mature subduction (i.e. a warmer slab centre), albeit driven by a distinct mechanism (i.e. along-strike variation in the DD).

4.4 Comparison with natural cases

The modelled along-strike changes in slab-top temperature are reflected, to first order, in geological observables extracted from some Earth subduction zones. Here, we provide a concise overview of a few such observations, but emphasize that our models correspond to highly idealized subduction. Natural comparisons are therefore mainly limited to qualitative trends.

The gradual cooling of the slab-top in our time-dependent models is supported by the exhumed rock record. Exhumed high pressure/low temperature oceanic rocks highlight extremely variable *P–T–t* conditions with, in general, warmer conditions during the early stages of subduction and an overall cooling trend as subduction progresses to more mature phases (e.g. Platt 1975; Cloos 1985; Krebs *et al.* 2008, 2011; Agard *et al.* 2018; Dragovic *et al.* 2020; Takeshita *et al.* 2023). This is consistent with the evolution of slab-top *P–T* conditions in our models (Fig. S8). These rocks reach peak pressures of up to 2.5 GPa (e.g. Beaumont *et al.* 1999; Jolivet *et al.* 2003; Yamato *et al.* 2007; Agard *et al.* 2009), and therefore correspond to depths of up to 100 km; at such depths in our models, the slab-top indeed cools rapidly.

Our models predict along-strike variability in slab-top temperatures, with a trend that varies from early to mature subduction zone. Although the modelled temperature contrast is low ($\leq$50 °C), the sense of variation agrees with that inferred from along-strike variations in exhumed rocks and arc magma geochemistry at some localities. During the earlier phases, our models predict colder slab centres due to elevated plate convergence. This is compatible with exhumed rock *P–T* constraints in the Aegean (in the Miocene) and Franciscan (in the late Jurassic–early Cretaceous) where, respectively, peak temperatures decrease by 100 °C (Jolivet *et al.* 2010) and up to 300 °C (e.g. Wakabayashi & Dumitru 2007; Ernst 2011) towards the centre of the system. Along-arc variation in magma geochemistry in the Sangihe arc has also been linked to a warmer slab edge (Hanyu *et al.* 2012). During mature subduction, where our models predict a warmer slab centre due to shallower DD, exhumation is typically linked to transient processes, such as large-scale changes in tectonic activity or slab break-off (e.g. Wang *et al.* 2023; Agard *et al.* 2018); isolating the modelled signal, even if present, is therefore challenging. However, the modelled, mature thermal variability is broadly consistent with that inferred from arc magma geochemistry in the Central Kamchatka Depression, with a plate centre proposed to be $\approx$150 °C warmer than the edges (Portnyagin & Manea 2008). We also inspected whether our modelled along-strike variations in DD would have a measurable effect on surface flux values in the forearc region of the overriding plate. There is negligible along-strike heat flux variation during the early subduction stages, when DD values are similar at the plate edge and centre (Fig. S9). However, during mature subduction, forearc heat flow at the edge of the subduction zone is $\sim$10 mW m^{-2} lower than that at the plate centre, as a result of the $\sim$5 km greater DD at the plate edge. This relationship between surface heat flow and DD agrees with Wada & Wang (2009) but, given measurement scatter and other sources of heat flow variability, the along-strike variation is likely too small to effectively use surface heat flow to detect DD variations of the magnitudes produced in our models.

Returning to along-strike trends in slab-top temperatures, there are, however, multiple subduction zones that do not match these trends; for example the Hikurangi Trench where Yabe *et al.* (2014) suggest that slab-top temperatures vary uniformly from edge to edge. The absolute values of modelled temperature variations are also much lower than these observational estimates. This may be due to the occurrence of more complex subduction geometries than within our models (and so more slab heating associated with toroidal flow) and/or the greater along-strike convergence rate changes (and so enhanced versions of the effects modelled here). Thus, further tailoring slab geometries and plate convergence to natural cases—and also incorporating additional mechanisms of heat transport and

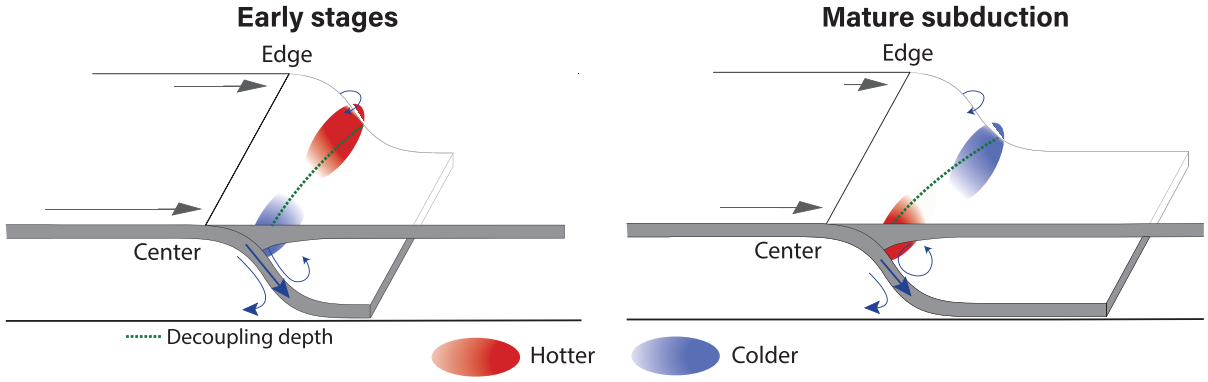

Figure 9. Illustration of the main study results. The length of the dark grey arrows indicates the magnitude of the plate velocity and the green dashed lines indicated the position of the decoupling depth.

production like small-scale convection (e.g. Honda & Saito 2003; Davies *et al.* 2016) and shear heating (e.g. Molnar & England 1990; Gao & Wang 2014)—would aid with a more direct comparison to specific cases. Shear heating, in particular, would also weaken the plate interface which could, in turn, elevate convergence rates (e.g. Behr & Becker 2018) and therefore affect slab-top temperature distribution. Our models, however, present an initial, idealized framework for the spatio-temporal variability of slab-top temperature.

5 CONCLUSIONS

Geological observations suggest that slab-top thermal structure simultaneously varies along strike and through time. To develop intuition about the drivers of this thermal variability, we developed time-dependent and dynamic 3-D subduction models. Specifically, we investigated the time dependence of the magnitude and sign of along-strike temperature variation for models with variable plate/slab widths (1000 km, 2000 km, infinite) and plate mobilities (fixed versus free subducting and overriding plates).

The along-strike temperature variation is heavily time-dependent but consistent between our models. In all cases, the region of the slab at the centre of the subduction system is colder than the slab edge by $\leq$35 °C during the early stages of subduction stages. During mature subduction, this trend reverses; the slab centre becomes warmer than the slab edge by $\leq$50 °C. During the early stages, the colder slab centre is due to more rapid convergence rates—and so less diffusive heating of the slab—at the centre of the subduction zone. During the mature stages, the slab centre is warmer as higher convergence rates begin to push the DD, and hence warm mantle material, to shallower depths than at the edge. Relative to some kinematically driven subduction modelling studies, our dynamic models generally predict lower along-strike temperature changes (tens instead of hundreds of degrees). This is due to a reduced role for toroidal flow-induced heating of the slab centre; deforming slabs, relatively wide trenches and near-orthogonal convergence reduce this effect in our models.

Relative to temperatures reconstructed from geological observations, our models generally predict comparable trends but reduced magnitudes of variation. More vigorous toroidal flow (e.g. due to more complex slab geometries) or greater along-strike variability in convergence rate (i.e. to produce more extreme DD variations) would likely reconcile this. Nevertheless, our models highlight new controls on 3-D slab-top temperatures that can only emerge with dynamic models: an important role for along-strike DD variations, and a time-dependent evolution of the sense of along-strike temperature variation.

ACKNOWLEDGMENTS

We are grateful to Laurent Husson and an anonymous reviewer for their helpful comments which improved the manuscript. We also thank the Computational Infrastructure for Geodynamics (geodynamics.org), which is funded by the National Science Foundation under awards EAR-0949446 and EAR-1550901, for supporting the development of ASPECT. This work used Stampede2 at TACC through allocation EAR180026 from the Extreme Science and Engineering Discovery Environment (XSEDE), which was supported by National Science Foundation grant number #1548562. AFH was partially supported by NSF EAR 2119842.

DATA AVAILABILITY STATEMENT

The ASPECT plugin, input geometries and parameter files necessary to run the models can be found in the following Zenodo repository: https://doi.org/10.5281/zenodo.8075606.

SUPPORTING INFORMATION

Supplementary data are available at *GJI* online.

suppl_data

Please note: Oxford University Press is not responsible for the content or functionality of any supporting materials supplied by the authors. Any queries (other than missing material) should be directed to the corresponding author for the paper.

REFERENCES

Agard, P., Yamato, P., Jolivet, L. & Burov, E., 2009. Exhumation of oceanic Blueschists and Eclogites in subduction zones: timing and mechanisms, *Earth-Sci. Rev.,* **92**(1–2), 53–79.

Agard, P., Plunder, A., Angiboust, S., Bonnet, G. & Ruh, J., 2018. The subduction plate interface: rock record and mechanical coupling (from long to short timescales), *Lithos,* **320–321,** 537–566.

Agard, P., Prigent, C., Soret, M., Dubacq, B., Guillot, S. & Deldicque, D., 2020. Slabitization: mechanisms controlling subduction development and viscous coupling, *Earth-Sci. Rev.,* **208,** doi:10.1016/j.earscirev.2020.103259.

Araya Vargas, J., Sanhueza, J. & Yáñez, G., 2021. The role of temperature in the along-margin distribution of volcanism and seismicity in subduction zones: insights from 3-D thermomechanical modeling of the Central Andean Margin, *Tectonics,* **40**(11), e2021TC006879.

Arcay, D., Tric, E. & Doin, M.-P., 2007. Slab surface temperature in subduction zones: influence of the interplate decoupling depth and upper plate thinning processes, *Earth planet. Sci. Lett.,* **255**(3–4), 324–338.

Bai, Y., Zhang, D., Dong, D., Wu, S. & Wang, Z., 2020. Aleutian island arc magma production rates and primary controlling factors, *Mar. Geol.,* **430,** doi:10.1016/j.margeo.2020.106346.

Bangerth, W., *et al.*, 2019. *ASPECT v2.1.0 [software]*.

Beaumont, C., Ellis, S. & Pfiffner, A., 1999. Dynamics of sediment subduction-accretion at convergent margins: short-term modes, long-term deformation, and tectonic implications, *J. geophys. Res.,* **104**(B8), 17 573–17 601.

Běhounková, M. & Čížková, H., 2008. Long-wavelength character of subducted slabs in the lower mantle, *Earth planet. Sci. Lett.,* **275**(1–2), 43–53.

Behr, W.M. & Becker, T.W., 2018. Sediment control on subduction plate speeds, *Earth planet. Sci. Lett.,* **502,** 166–173.

Behr, W.M., Holt, A.F., Becker, T.W. & Faccenna, C., 2022. The effects of plate interface rheology on subduction kinematics and dynamics, *Geophys. J. Int.,* **230**(2), 796–812.

Bengtson, A.K. & van Keken, P.E., 2012. Three-dimensional thermal structure of subduction zones: effects of obliquity and curvature, *Solid Earth,* **3**(2), 365–373.

Capitanio, F.A., Stegman, D.R., Moresi, L.-N. & Sharples, W., 2010. Upper plate controls on deep subduction, trench migrations and deformations at convergent margins, *Tectonophysics,* **483**(1-2), 80–92.

Christensen, U.R., 1996. The influence of trench migration on slab penetration into the lower mantle, *Earth planet. Sci. Lett.,* **140**(1–4), 27–39.

Cloos, M., 1985. Thermal evolution of convergent plate margins: thermal modeling and reevaluation of isotopic Ar-ages for blueschists in the franciscan complex of California, *Tectonics,* **4**(5), 421–433.

Davies, D., Le Voci, G., Goes, S., Kramer, S.C. & Wilson, C.R., 2016. The mantle wedge's transient 3-D flow regime and thermal structure, *Geochem. Geophys. Geosyst.,* **17**(1), 78–100.

Dhar, S., Muto, J., Ito, Y., Miura, S., Moore, J.D., Ohta, Y. & Iinuma, T., 2022. Along-arc heterogeneous rheology inferred from post-seismic deformation of the 2011 Tohoku-Oki earthquake, *Geophys. J. Int.,* **230**(1), 202–215.

Di Giuseppe, E., Van Hunen, J., Funiciello, F., Faccenna, C. & Giardini, D., 2008. Slab stiffness control of trench motion: insights from numerical models, *Geochem. Geophys. Geosyst.,* **9**(2), doi:10.1029/2007GC001776.

Dragovic, B., Angiboust, S. & Tappa, M.J., 2020. Petrochronological close-up on the thermal structure of a paleo-subduction zone (W. Alps), *Earth planet. Sci. Lett.,* **547,** doi:10.1016/j.epsl.2020.116446.

Elburg, M. & Foden, J., 1998. Temporal changes in arc magma geochemistry, Northern Sulawesi, Indonesia, *Earth planet. Sci. Lett.,* **163**(1–4), 381–398.

Enns, A., Becker, T.W. & Schmeling, H., 2005. The dynamics of subduction and trench migration for viscosity stratification, *Geophys. J. Int.,* **160**(2), 761–775.

Ernst, W., 1973. Blueschist metamorphism and P-T regimes in active subduction zones, *Tectonophysics,* **17**(3), 255–272.

Ernst, W., 2011. Accretion of the Franciscan complex attending Jurassic–Cretaceous geotectonic development of northern and central California, *Bulletin,* **123**(9-10), 1667–1678.

Faccenda, M. & Capitanio, F.A., 2012. Development of mantle seismic anisotropy during subduction-induced 3-D flow, *Geophys. Res. Lett.,* **39**(11), doi:10.1029/2012GL051988.

Funiciello, F., Morra, G., Regenauer-Lieb, K. & Giardini, D., 2003. Dynamics of retreating slabs: 1. Insights from two-dimensional numerical experiments, *J. geophys. Res.,* **108**(B4), doi:10.1029/2001JB000898.

Furukawa, Y., 1993. Depth of the decoupling plate interface and thermal structure under arcs, *J. geophys. Res.,* **98**(B11), 20 005–20 013.

Gao, X. & Wang, K., 2014. Strength of stick-slip and creeping subduction megathrusts from heat flow observations, *Science,* **345**(6200), 1038–1041.

Hager, B.H., 1984. Subducted slabs and the geoid: constraints on mantle rheology and flow, *J. geophys. Res.,* **89**(B7), 6003–6015.

Hanyu, T. *et al.*, 2012. Across-and along-arc geochemical variations of lava chemistry in the Sangihe Arc: various fluid and melt slab fluxes in response to slab temperature, *Geochem. Geophys. Geosyst.,* **13**(10), doi:10.1029/2012GC004346.

Heister, T., Dannberg, J., Gassmöller, R. & Bangerth, W., 2017. High accuracy mantle convection simulation through modern numerical methods. II: realistic models and problems, *Geophys. J. Int.,* **210**(2), 833–851.

Hirauchi, K.-I. & Katayama, I., 2013. Rheological contrast between serpentine species and implications for slab–mantle wedge decoupling, *Tectonophysics,* **608,** 545–551.

Hirth, G. & Kohlstedt, D., 2003. Rheology of the upper mantle and the mantle wedge: a view from the experimentalists, *Geophys. Monogr.-AGU,* **138,** 83–106.

Holt, A.F. & Condit, C.B., 2021. Slab temperature evolution over the lifetime of a subduction zone, *Geochem. Geophys. Geosyst.,* **22**(6), e2020GC009476.

Holt, A.F., Becker, T. & Buffett, B., 2015. Trench migration and overriding plate stress in dynamic subduction models, *Geophys. J. Int.,* **201**(1), 172–192.

Honda, S. & Saito, M., 2003. Small-scale convection under the back-arc occurring in the low viscosity wedge, *Earth planet. Sci. Lett.,* **216**(4), 703–715.

Jadamec, M.A. & Billen, M.I., 2010. Reconciling surface plate motions with rapid three-dimensional mantle flow around a slab edge, *Nature,* **465**(7296), 338–341.

Ji, Y., Yoshioka, S. & Matsumoto, T., 2016. Three-dimensional numerical modeling of temperature and mantle flow fields associated with subduction of the Philippine Sea Plate, southwest Japan, *J. geophys. Res.,* **121**(6), 4458–4482.

Ji, Y., Yoshioka, S., Manea, V.C., Manea, M. & Matsumoto, T., 2017. Three-dimensional numerical modeling of thermal regime and slab dehydration beneath Kanto and Tohoku, Japan, *J. geophys. Res.,* **122**(1), 332–353.

Jolivet, L., Faccenna, C., Goffé, B., Burov, E. & Agard, P., 2003. Subduction tectonics and exhumation of high-pressure metamorphic rocks in the mediterranean orogens, *Am. J. Sci.,* **303**(5), 353–409.

Jolivet, L., Trotet, F., Monié, P., Vidal, O., Goffé, B., Labrousse, L., Agard, P. *et al.*, 2010. Along-strike variations of P–T conditions in accretionary wedges and syn-orogenic extension, the HP–LT Phyllite–Quartzite Nappe in Crete and the Peloponnese, *Tectonophysics,* **480**(1–4), 133–148.

Katili, J.A., 1975. Volcanism and plate tectonics in the Indonesian Island Arcs, *Tectonophysics,* **26**(3–4), 165–188.

Kerswell, B.C., Kohn, M.J. & Gerya, T.V., 2021. Backarc lithospheric thickness and serpentine stability control slab-mantle coupling depths in subduction zones, *Geochem. Geophys. Geosyst.,* **22**(6), e2020GC009304.

Kincaid, C. & Griffiths, R., 2003. Laboratory models of the thermal evolution of the mantle during rollback subduction, *Nature,* **425**(6953), 58–62.

Kincaid, C. & Griffiths, R., 2004. Variability in flow and temperatures within mantle subduction zones, *Geochem. Geophys. Geosyst.,* **5**(6), doi:10.1029/2003GC000666.

Kincaid, C. & Olson, P., 1987. An experimental study of subduction and slab migration, *J. geophys. Res.,* **92**(B13), 13 832–13 840.

Kincaid, C. & Sacks, I.S., 1997. Thermal and dynamical evolution of the upper mantle in subduction zones, *J. geophys. Res.,* **102**(B6), 12 295–12 315.

Kirby, S., Engdahl, R.E. & Denlinger, R., 1996. Intermediate-depth intraslab earthquakes and arc volcanism as physical expressions of crustal and uppermost mantle metamorphism in subducting slabs, in *Subduction: Top to Bottom,* Vol. **96,** pp. 195–214, eds Bebout, Gray E., Scholl, David W., Kirby, Stephen H. & Platt, John P., AGU.

Kneller, E.A. & van Keken, P.E., 2008. Effect of three-dimensional slab geometry on deformation in the mantle wedge: implications for shear wave anisotropy, *Geochem. Geophys. Geosyst.,* **9**(1), doi:10.1029/2007GC001677.

Krebs, M., Maresch, W., Schertl, H.-P., Münker, C., Baumann, A., Draper, G., Idleman, B. & Trapp, E., 2008. The dynamics of intra-oceanic subduction zones: a direct comparison between fossil petrological evidence (Rio San Juan Complex, Dominican Republic) and numerical simulation, *Lithos,* **103**(1–2), 106–137.

Krebs, M., Schertl, H.-P., Maresch, W. & Draper, G., 2011. Mass flow in serpentinite-hosted subduction channels: P–T–T path patterns of metamorphic blocks in the Rio San Juan MéLange (Dominican Republic), *J. Asian Earth Sci.,* **42**(4), 569–595.

Kronbichler, M., Heister, T. & Bangerth, W., 2012. High accuracy mantle convection simulation through modern numerical methods, *Geophys. J. Int.,* **191,** 12–29.

Maunder, B., van Hunen, J., Bouilhol, P. & Magni, V., 2019. Modeling slab temperature: a reevaluation of the thermal parameter, *Geochem. Geophys. Geosyst.,* **20**(2), 673–687.

Molnar, P. & England, P., 1990. Temperatures, heat flux, and frictional stress near major thrust faults, *J. geophys. Res.,* **95**(B4), 4833–4856.

Morishige, M. & van Keken, P.E., 2014. Along-arc variation in the 3-D thermal structure around the junction between the Japan and Kurile Arcs, *Geochem. Geophys. Geosyst.,* **15**(6), 2225–2240.

O'Brien, P.J., 1997. Garnet zoning and reaction textures in overprinted eclogites, Bohemian Massif, European Variscides: a record of their thermal history during exhumation, *Lithos,* **41**(1–3), 119–133.

Peacock, S.M., 1996. Thermal and petrologic structure of subduction zones, in *Subduction: Top To Bottom,* Vol. **96,** pp. 119–133, eds Bebout, Gray E., Scholl, David W., Kirby, Stephen H. & Platt, John P., AGU.

Peacock, S.M. & Wang, K., 1999. Seismic consequences of warm versus cool subduction metamorphism: examples from southwest and northeast japan, *Science,* **286**(5441), 937–939.

Peacock, S.M. & Wang, K., 2021. On the stability of talc in subduction zones: a possible control on the maximum depth of decoupling between the subducting plate and mantle wedge, *Geophys. Res. Lett.,* **48**(17), e2021GL094889.

Perrin, A., Goes, S., Prytulak, J., Rondenay, S. & Davies, D.R., 2018. Mantle wedge temperatures and their potential relation to volcanic arc location, *Earth planet. Sci. Lett.,* **501,** 67–77.

Piromallo, C., Becker, T., Funiciello, F. & Faccenna, C., 2006. Three-dimensional instantaneous mantle flow induced by subduction, *Geophys. Res. Lett.,* **33**(8), doi:10.1029/2005GL025390.

Platt, J., 1975. Metamorphic and deformational processes in the Franciscan Complex, California: some insights from the Catalina Schist Terrane, *Bull. geol. Soc. Am.,* **86**(10), 1337–1347.

Plunder, A., Thieulot, C. & Van Hinsbergen, D.J., 2018. The effect of obliquity on temperature in subduction zones: insights from 3-D numerical modeling, *Solid Earth,* **9**(3), 759–776.

Portnyagin, M. & Manea, V.C., 2008. Mantle temperature control on composition of arc magmas along the central Kamchatka depression, *Geology,* **36**(7), 519–522.

Quinquis, M.E., Buiter, S.J. & Ellis, S., 2011. The role of boundary conditions in numerical models of subduction zone dynamics, *Tectonophysics,* **497**(1–4), 57–70.

Schellart, W., 2004. Kinematics of subduction and subduction-induced flow in the upper mantle, *J. geophys. Res.,* **109**(B7), doi:10.1029/2004JB002970.

Schellart, W. & Moresi, L., 2013. A new driving mechanism for backarc extension and backarc shortening through slab sinking induced toroidal and poloidal mantle flow: results from dynamic subduction models with an overriding plate, *J. geophys. Res.,* **118**(6), 3221–3248.

Sleep, N. & Toksöz, M.N., 1971. Evolution of marginal basins, *Nature,* **233**(5321), 548–550.

Stegman, D., Freeman, J., Schellart, W.P., Moresi, L. & May, D., 2006. Influence of trench width on subduction hinge retreat rates in 3-D models of slab rollback, *Geochem. Geophys. Geosyst.,* **7**(3), doi:10.1029/2005GC001056.

Stegman, D., Schellart, W. & Freeman, J., 2010. Competing influences of plate width and far-field boundary conditions on trench migration and morphology of subducted slabs in the upper mantle, *Tectonophysics,* **483**(1–2), 46–57.

Stein, C.A. & Stein, S., 1992. A model for the global variation in oceanic depth and heat flow with lithospheric age, *Nature,* **359**(6391), 123–129.

Syracuse, E.M., van Keken, P.E. & Abers, G.A., 2010. The global range of subduction zone thermal models, *Phys. Earth planet. Inter.,* **183**(1–2), 73–90.

Takeshita, T., Imayama, T., Ando, M., Kimura, Y. & Python, M., 2023. Pressure–temperature paths of tectonic blocks in mélange: recording thermal evolution of a subduction channel at an initial stage of subduction, *J. Metamor. Geol.,* **41**(6), 787–816.

Tupinambá, M., Heilbron, M., Valeriano, C., Júnior, R.P., de Dios, F.B., Machado, N., do Eirado Silva, L.G. & de Almeida, J. C.H., 2012. Juvenile contribution of the Neoproterozoic Rio Negro magmatic arc (Ribeira Belt, Brazil): implications for western Gondwana amalgamation, *Gondw. Res.,* **21**(2), 422–438.

Turcotte, D.L. & Schubert, G., 2002. *Geodynamics,* Cambridge Univ. Press.

Van Keken, P.E., Kiefer, B. & Peacock, S.M., 2002. High-resolution models of subduction zones: implications for mineral dehydration reactions and the transport of water into the deep mantle, *Geochem. Geophys. Geosyst.,* **3**(10), 1–20.

van Keken, P.E., Hacker, B.R., Syracuse, E.M. & Abers, G.A., 2011. Subduction factory: 4. Depth-dependent flux of H_2O from subducting slabs worldwide, *J. geophys. Res.,* **116**(B1), doi:10.1029/2010JB007922.

Wada, I., 2021. A simple picture of mantle wedge flow patterns and temperature variation, *J. Geodyn.,* **146,** doi:10.1016/j.jog.2021.101848.

Wada, I. & He, J., 2017. Thermal structure of the Kanto Region, Japan, *Geophys. Res. Lett.,* **44**(14), 7194–7202.

Wada, I. & Wang, K., 2009. Common depth of slab-mantle decoupling: reconciling diversity and uniformity of subduction zones, *Geochem. Geophys. Geosyst.,* **10**(10), doi:10.1029/2009GC002570.

Wada, I., Wang, K., He, J. & Hyndman, R.D., 2008. Weakening of the subduction interface and its effects on surface heat flow, slab dehydration, and mantle wedge serpentinization, *J. geophys. Res.,* **113**(B4), doi:10.1029/2007JB005190.

Wada, I., He, J., Hasegawa, A. & Nakajima, J., 2015. Mantle wedge flow pattern and thermal structure in northeast Japan: effects of oblique subduction and 3-D slab geometry, *Earth planet. Sci. Lett.,* **426,** 76–88.

Wakabayashi, J. & Dumitru, T.A., 2007. 40Ar/39Ar ages from coherent, high-pressure metamorphic rocks of the Franciscan Complex, California: revisiting the timing of metamorphism of the world's type subduction complex, *Int. Geol. Rev.,* **49**(10), 873–906.

Wang, Y., Wang, K., He, J. & Zhang, L., 2023. On unusual conditions for the exhumation of subducted oceanic crustal rocks: how to make rocks hotter than models, *Earth planet. Sci. Lett.,* **615,** doi:10.1016/j.epsl.2023.118213.

Wiens, D.A., 2001. Seismological constraints on the mechanism of deep earthquakes: temperature dependence of deep earthquake source properties, *Phys. Earth planet. Inter.,* **127**(1–4), 145–163.

Yabe, S., Ide, S. & Yoshioka, S., 2014. Along-strike variations in temperature and tectonic tremor activity along the Hikurangi Subduction Zone, new zealand, *Earth, Planets Space,* **66**(1), 1–15.

Yamato, P., Agard, P., Burov, E., Le Pourhiet, L., Jolivet, L. & Tiberi, C., 2007. Burial and exhumation in a subduction wedge: mutual constraints from thermomechanical modeling and natural P-T-T data (Schistes LustréS, western Alps), *J. geophys. Res.,* **112**(B7), doi:10.1029/2006JB004441.

Yamato, P., Husson, L., Braun, J., Loiselet, C. & Thieulot, C., 2009. Influence of surrounding plates on 3D subduction dynamics, *Geophys. Res. Lett.,* **36**(7), doi:10.1029/2008GL036942.

Zhou, X. & Wada, I., 2021. Differentiating induced versus spontaneous subduction initiation using thermomechanical models and metamorphic soles, *Nat. Commun.,* **12**(1), doi:10.1038/s41467-021-24896-x